

# Study on the Corrosion Resistance of Superhydrophobic Ni-Co-P-BN(h) Nanocomposite Coatings Prepared by Electrochemical Machining and Fluorosilane Modification

Yin Zhang<sup>1</sup>, Min Kang<sup>1,2,\*</sup>, Meifu Jin<sup>1,2</sup>, Nyambura Samuel Mbugua<sup>1</sup>, Jiping Zhu<sup>3</sup>

<sup>1</sup> College of Engineering, Nanjing Agricultural University, Nanjing, 210031, China;

<sup>2</sup> Guanyun Research Institute for Modern Agricultural Equipment, Nanjing Agricultural University, Guanyun, 222200, China;

<sup>3</sup> Nanjing Institute of Agricultural Mechanization, Ministry of Agriculture and Rural Affairs, Nanjing, 210008, China;

\*E-mail: [kangmin@njau.edu.cn](mailto:kangmin@njau.edu.cn)

Received: 6 November 2019 / Accepted: 30 December 2019 / Published: 10 February 2020

---

In this work, a superhydrophobic surface was fabricated on 45 steel substrates by using electrochemical machining to improve the corrosion resistance of Ni-Co-P-BN(h) nanocomposite coatings. The surface morphology, chemical composition, crystalline structure, surface roughness and wettability of the samples were investigated with scanning electron microscopy (SEM), energy dispersive spectroscopy (EDS), X-ray diffraction (XRD), laser scanning confocal microscopy (LSCM) and water contact angle measurements, respectively. The corrosion resistance of the samples was investigated in a 3.5 wt% NaCl solution using an electrochemical workstation. The results showed that the current density and processing time in electrochemical machining significantly influenced the wettability. The Ni-Co-P-BN(h) nanocomposite coatings exhibited a superhydrophobic surface under suitable process parameters. Evaluation of this superhydrophobic surface revealed an average water contact angle of 153.2° and a sliding angle of 5° in the contact angle test. In addition, the polarization curve in the electrochemical test indicated that the superhydrophobic surface exhibited a lower corrosion current density ( $I_{\text{corr}}$ ) of 0.14  $\mu\text{A}/\text{cm}^2$  and a higher polarization resistance ( $R_p$ ) of 131.40  $\text{k}\Omega \cdot \text{cm}^2$  when compared with those of the normal samples. The above results showed that Ni-Co-P-BN(h) nanocomposite coatings with superhydrophobic surfaces could provide improved corrosion resistance.

---

**Keywords:** Electrochemical machining, Ni-Co-P-BN(h) nanocomposite coatings, Surface roughness, Wettability, Corrosion resistance

## 1. INTRODUCTION

It is worth noting that metals are susceptible to corrosion and wear in major engineering and daily life, which poses a serious threat to daily life and can cause environmental contamination, financial

loss and social harm [1-2]. Much research has been carried out to identify efficient methods for protecting metals and alloys from corrosion. To date, organic coatings are one of the most economical, practical and common protective measures. They can provide a barrier between the surrounding corrosive environment and the metal surface, prolonging the service life of the substrate materials [3].

Ni-Co-P alloy coatings have high hardness, wear resistance, corrosion resistance, permeability and saturation magnetization. They are widely used as anti-corrosion materials, diffusion barriers and electrocatalytic materials [4]. Fetohi reported that Ni-Co-P coatings have lower corrosion current densities and more positive corrosion potentials than those of Ni-P coatings, thus, Ni-Co-P coatings show much better corrosion resistance [5]. In addition, a variety of nanocomposites with different nanoparticles have been reported that enhance the corrosion resistance of substrate materials, such as TiO<sub>2</sub> [6], CeO<sub>2</sub> [7], SiC [8], rGO [9], BN [10, 11], SnO<sub>2</sub> [12], CNTs [13], Si<sub>3</sub>N<sub>4</sub> [14], and TiN [15]. Hexagonal boron nitride (BN(h)) with a graphite-like structure has excellent properties, such as stability at high temperature, a low friction coefficient, and a low wear rate and lubricity, thus showing promising potential as a reinforcing phase for composite coatings [16]. Therefore, studies on Ni-Co-P-BN(h) nanocomposite coatings with BN(h) as a second phase have great significance and value in the improvement of material surface properties.

In recent years, superhydrophobic surfaces (SHSs) with a contact angle (CA) larger than 150° and a sliding angle (SA) smaller than 10° have attracted much research interest due to their remarkable properties [17, 18], including anti-corrosion [19-20], self-cleaning [21], oil-water separating [22], anti-icing [23], drag-reducing [24], and anti-fouling [25]; they have even been used as antibacterial coatings [26]. It has been confirmed that low surface energy and proper surface roughness are two key factors in the preparation of superhydrophobic surfaces [27-28]. At present, many methods have been reported for fabricating SHSs, including laser treatment [29], three-dimensional printing [30], self-assembly [31], dipping [32], anodizing [33], plasma treatment [34], chemical etching [35-36], electron discharge machining [37], and electrochemical deposition [38-39]. However, most of the mentioned methods usually suffer from certain limitations, such as high cost, use of expensive equipment, strict process control, complex engineering procedures, long fabrication times, and instability; furthermore, they may be unsuitable for large-scale production and inapplicable for arbitrarily shaped surfaces, which limits their applications in real life. The electrochemical machining method is used in this work due to its simplicity, high effectiveness, efficiency, low cost, relatively easy operation, convenient repetition and ability to make large-area superhydrophobic surfaces for substrates with different shapes [40-41].

In this work, we attempt to fabricate superhydrophobic Ni-Co-P-BN(h) nanocomposite coatings on 45 steel substrates by electrochemical machining under a suitable current density and processing time to improve the anti-corrosion protection of the metal. The surface morphology, chemical composition, crystalline structure, surface roughness, wettability and corrosion resistance of Ni-Co-P-BN(h) nanocomposite coatings are characterized and analysed by scanning electron microscopy (SEM), energy dispersive spectroscopy (EDS), X-ray diffraction (XRD), laser scanning confocal microscopy (LSCM), contact angle measurement of the optical surface and electrochemical workstation tests. The above tests and analysis results may be useful to improve the corrosion resistance of Ni-Co-P-BN(h) nanocomposite coatings and provide a theoretical basis for their future application.

## 2. EXPERIMENTAL

### 2.1. Materials and pretreatments

The substrate in this study was 45 steel (size: 30 mm× 8 mm× 7 mm), which was purchased from Suzhou Co. (Jiangsu, China), with the following composition: C 0.46%, Si 0.27%, Cr 0.05%, Ni 0.04%, Mn 0.59%, P 0.02%, Cu 0.05% and S 0.02%. A type 45 steel substrate usually requires a series of pretreatment steps to ensure good quality deposition. First, the 45 steel substrates were cleaned and polished by #320 WC sandpaper. Further abrading with grades #800 to #1500 WC sandpaper obtained a bright and smooth surface. Then, the 45 steel substrates were treated by electrochemical degreasing to remove oil contamination in a solution containing 25 g·L<sup>-1</sup> NaOH, 21.7 g·L<sup>-1</sup> Na<sub>2</sub>CO<sub>3</sub>, 50 g·L<sup>-1</sup> Na<sub>3</sub>PO<sub>4</sub> and 2.4 g·L<sup>-1</sup> NaCl. The treatment current was 1 A, and the processing time was 25 s. Third, the 45 steel substrates were immersed into a strong activation solution containing 25 g·L<sup>-1</sup> hydrochloric acid and 140.1 g·L<sup>-1</sup> NaCl for the removal of the oxide film from the surface. The strong activation treatment current was 1 A, and the processing time was 30 s. Finally, the 45 steel substrates were immersed in a weak activation solution containing 141.2 g·L<sup>-1</sup> Na<sub>3</sub>C<sub>6</sub>H<sub>5</sub>O<sub>7</sub>·2H<sub>2</sub>O, 94.3 g·L<sup>-1</sup> H<sub>3</sub>C<sub>6</sub>H<sub>5</sub>O<sub>7</sub>·H<sub>2</sub>O and 3.0 g·L<sup>-1</sup> NiCl<sub>2</sub>·6H<sub>2</sub>O for the removal of carbon black from the surface. The weak activation treatment current was 1 A, and the processing time was 30 s. In between every step, the 45 steel substrates were rinsed with deionized water and air dried.

### 2.2 Preparation of the Ni-Co-P-BN(h) nanocomposite coating

The Ni-Co-P-BN(h) nanocomposite coatings were fabricated on the 45 steel substrates via electrodeposition in a modified Watts bath with an aqueous solution containing 200 g·L<sup>-1</sup> NiSO<sub>4</sub>·6 H<sub>2</sub>O, 30 g·L<sup>-1</sup> NiCl<sub>2</sub>·6 H<sub>2</sub>O, 20 g·L<sup>-1</sup> CoSO<sub>4</sub>·7 H<sub>2</sub>O, 30 g·L<sup>-1</sup> H<sub>3</sub>BO<sub>3</sub>, 20 g·L<sup>-1</sup> H<sub>3</sub>PO<sub>3</sub>, 60 g·L<sup>-1</sup> C<sub>6</sub>H<sub>8</sub>O<sub>7</sub>, 0.08 g·L<sup>-1</sup> sodium dodecyl sulfate, 0.02 g·L<sup>-1</sup> sulphourea and 8 g·L<sup>-1</sup> BN(h) with average particle sizes of 50 nm, 100 nm, 500 nm and 800 nm. Specifically, a 99.9% pure nickel electrode (size: 200 mm×50 mm×5 mm) was used as an anode. The cathode was one of the 45 steel substrates mounted parallel to the anode plate. In the electrodeposition process, the temperature of the plating solution was maintained at 60 °C, and the speed of magnetic stirring was 300 rpm. The duration of the electrodeposition was 90 min with a current density of 6 A·dm<sup>-2</sup>.

### 2.3 Preparation of the hydrophobic surfaces

To obtain a superhydrophobic surface, the Ni-Co-P-BN(h) nanocomposite coatings were treated by electrochemical machining (ECM) and fluoroalkyl silane (FAS). In the electrochemical machining, the samples plated with Ni-Co-P-BN(h) nanocomposite coatings were used as anodes, and a 99.9% pure nickel plate was used as the cathode in a 0.1 mol·L<sup>-1</sup> NaCl solution. The electrochemical machining method used a DC voltage at 25 °C. The operation was carried out at various current densities (5 A·dm<sup>-2</sup>, 10 A·dm<sup>-2</sup>, 15 A·dm<sup>-2</sup>, 20 A·dm<sup>-2</sup> and 25 A·dm<sup>-2</sup>) and with different processing times (0 s, 30 s, 60 s, 90 s and 120 s). The fluoroalkyl silane alcohol solution was comprised of fluorosilane (2%) and absolute

alcohol (98%), which were placed in a beaker and stirred for 6 h at 800 rpm. The FAS alcohol solution needed to rest for 12 h at 25 °C before being used. It was necessary for all samples to be dry and dust-free prior to modification by FAS. The samples were soaked in the FAS alcohol solution for 2 h without stirring. The modified samples were dried in a drying oven for 1 h at 120 °C.

#### 2.4 Characterization and tests

The surface morphologies and cross-sections of the Ni-Co-P-BN(h) nanocomposite coatings were observed by using scanning electron microscopy (SEM, Quanta 250, FEI, Hillsboro, OR, USA), and the chemical compositions were analysed by energy dispersive spectroscopy (EDS, OXFORD X-MAX 20 mm<sup>2</sup>, UK). The crystalline structures of the Ni-Co-P-BN(h) nanocomposite coatings were analysed by X-ray diffraction (XRD, X'Pert Powder, PANalytical B.V., Almelo, Holland). The X-ray source used was Cu K $\alpha$  radiation ( $\lambda=0.154056$  nm) and was operated at 40 kV within a range of 20 to 90° at a scanning rate of  $2\theta=4^\circ/\text{min}$ . The surface roughness  $S_a$  was measured by laser scanning confocal microscopy (LSCM, OLS4000, OLYMPUS, Japan). The roughness corresponded to the average value measured at five separate points. The static contact angle (CA) was measured by a contact angle meter (OCA15EC, Dataphysics, Germany). Water droplets (3  $\mu\text{L}$ ) were carefully dropped onto the surface of the samples, the water droplet velocity was 1  $\mu\text{L}/\text{s}$ , and the average value of five measurements obtained at different positions on the samples was adopted as the final contact angle. The corrosion resistance of the samples was tested by an electrochemical workstation (CS350, Wuhan Corrtest Instruments Corp., Ltd., Wuhan, China). Typically, the samples, platinum plate, and saturated calomel electrode were considered the working electrode, counter electrode and reference electrode, respectively. The exposure area of the working electrode was 1 cm<sup>2</sup>. To obtain a stable system, the samples were immersed in a 3.5 wt% NaCl aqueous solution for 0.5 h before the electrochemical experiments. Afterwards, the potential dynamic sweeping range was performed in a potential range of  $\pm 0.6$  V with respect to the  $E_{\text{ocp}}$  at a 0.5 mV/s sweeping rate.

### 3. RESULTS AND DISCUSSION

#### 3.1 Surface morphologies, cross-sectional images, XRD and EDS of the Ni-Co-P-BN(h) nanocomposite coatings

Figure 1 shows the surface morphologies of the Ni-Co-P-BN(h) nanocomposite coatings with differently sized BN(h) particles. Figure 2 presents the cross-sectional images of the Ni-Co-P-BN(h) nanocomposite coatings with differently sized BN(h) particles. After comparing Figures 1 and 2, the BN(h) particle size had little influence on the surface morphology and thickness of the Ni-Co-P-BN(h) nanocomposite coatings. Furthermore, the figures showed that the coatings had no cracks and exhibited dense structures. In addition, the thickness of the Ni-Co-P-BN(h) nanocomposite coatings with BN(h) particle sizes of 50 nm, 100 nm, 500 nm and 800 nm increased to 37.72  $\mu\text{m}$ , 37.94  $\mu\text{m}$ , 38.85  $\mu\text{m}$  and 38.93  $\mu\text{m}$ , respectively.

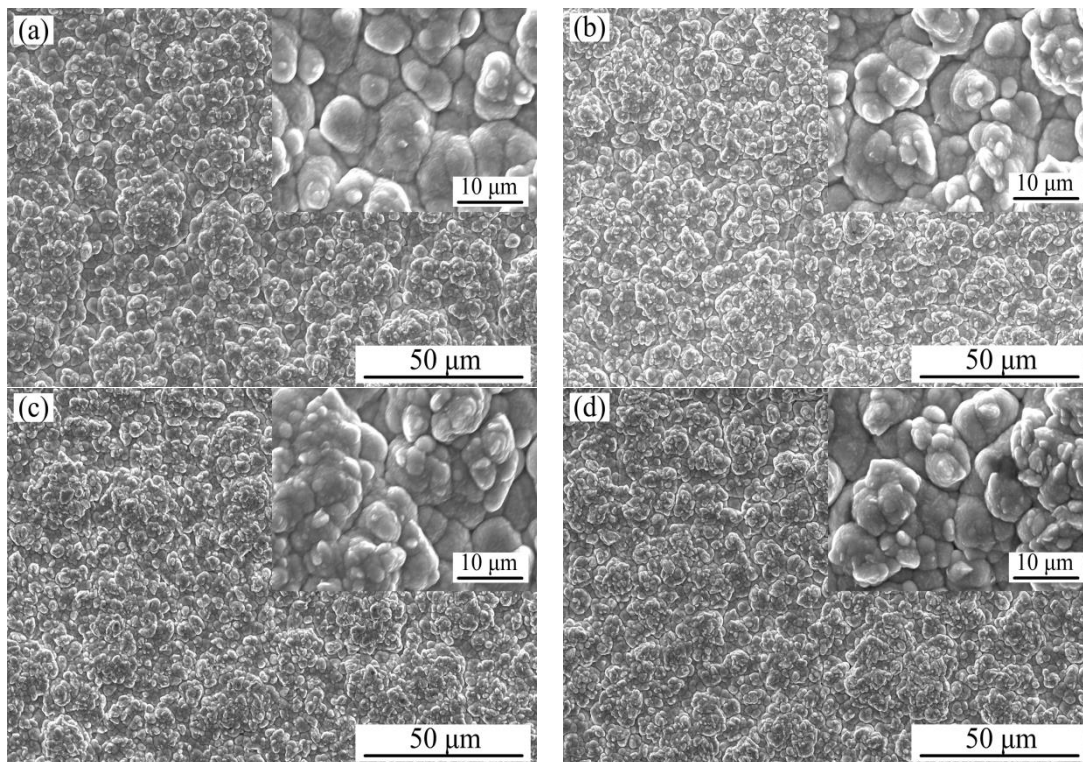


**Figure 1.** Surface morphologies of the samples with differently sized BN(h) particles: (a) 50 nm, (b) 100 nm, (c) 500 nm, and (d) 800 nm (60 °C, 6 A·dm<sup>-2</sup>, 90 min and 300 rpm).

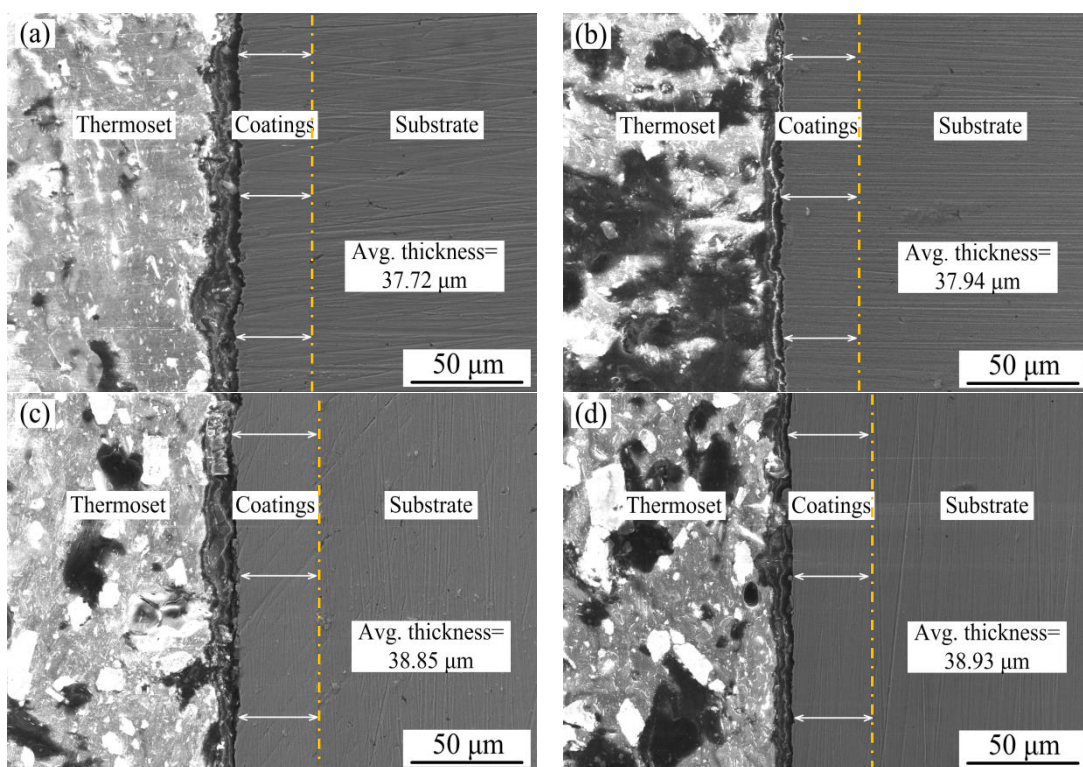


**Figure 2.** Cross-sectional images of the samples with differently sized BN(h) particles: (a) 50 nm, (b) 100 nm, (c) 500 nm, and (d) 800 nm (60 °C, 6 A·dm<sup>-2</sup>, 90 min and 300 rpm).

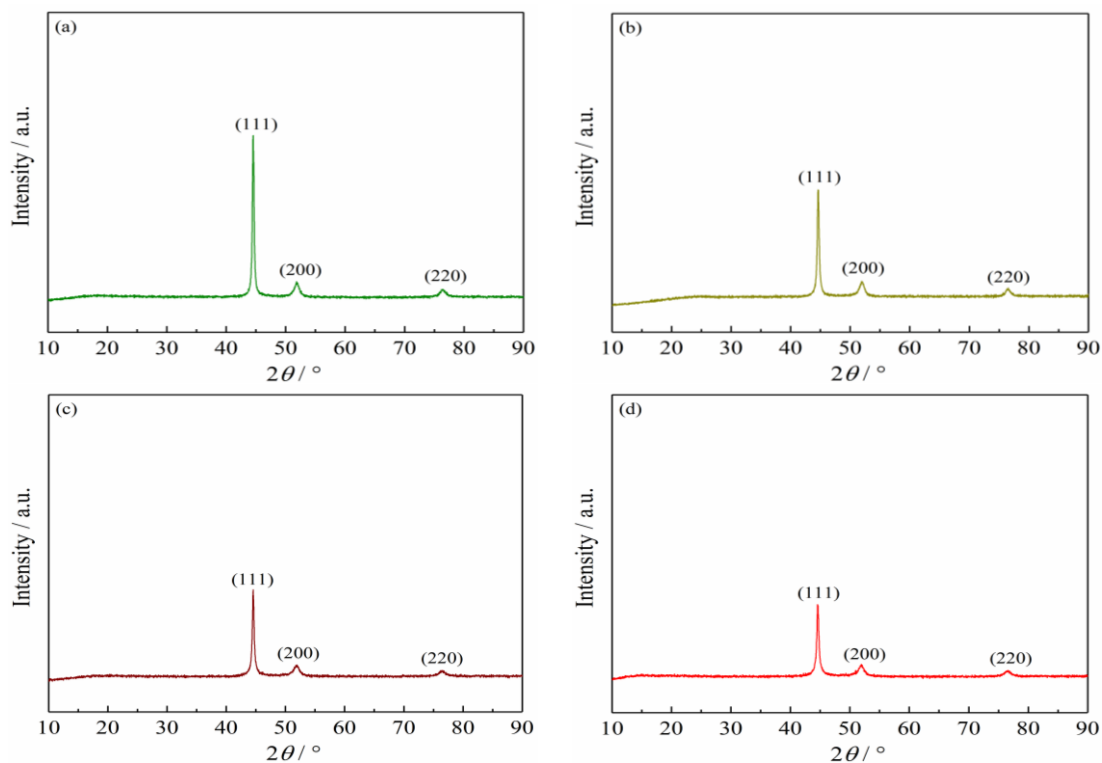


**Figure 3.** XRD patterns of the samples with differently sized BN(h) particles: (a) 50 nm, (b) 100 nm, (c) 500 nm and (d) 800 nm (60 °C, 6 A·dm<sup>-2</sup>, 90 min and 300 rpm).

The XRD patterns of the Ni-Co-P-BN(h) nanocomposite coatings with differently sized BN(h) particles (a) 50 nm, (b) 100 nm, (c) 500 nm and (d) 800 nm, are presented in Figure 3.

**Table 1.** Calculated crystallite size by the Scherrer equation for the Ni-Co-P-BN(h) nanocomposite coatings with differently sized BN(h) particles: 50 nm, 100 nm, 500 nm and 800 nm

Samples	Hkl plane	2θ	θ	FWHM	Grain size / nm
BN(h) 50 nm	111	44.501	22.250	0.347	24.473
	200	51.738	25.869	0.955	
	220	76.455	38.227	0.704	
BN(h) 100 nm	111	44.589	22.294	0.386	22.007
	200	51.885	25.942	0.905	
	220	76.416	38.208	0.793	
BN(h) 500 nm	111	44.519	22.259	0.409	20.764
	200	51.795	25.897	1.048	
	220	76.369	38.184	1.001	
BN(h) 800 nm	111	44.574	22.287	0.428	19.847
	200	51.786	25.893	1.093	
	220	76.473	38.236	0.961	

It was observed that the crystal planes of the three diffraction peaks are (111), (200) and (220). The structure was a face-centred cubic structure. The diffraction intensities of the (111) fibre orientations decreased as the BN(h) sizes increased in the Ni-Co-P-BN(h) nanocomposite coatings . The grain sizes

for the coatings were derived from the Scherrer equation, as shown in Table 1. The average grain diameters of the Ni-Co-P-BN(h) nanocomposite coatings with differently sized BN(h) particles of (a) 50 nm, (b) 100 nm, (c) 500 nm and (d) 800 nm, were 24.473 nm, 22.007 nm, 20.764 nm and 19.847 nm, respectively.

Figure 4 shows the EDS spectra of the samples with differently sized BN(h) particles of (a) 50 nm, (b) 100 nm, (c) 500 nm and (d) 800 nm. As shown in Figure 4, which revealed the presence of Ni, Co, P, B and N, the Ni contents of the samples with BN(h) particle sizes of 50 nm, 100 nm, 500 nm and 800 nm were 76.8 wt%, 76.5 wt%, 76.6 wt% and 77.3 wt%, respectively. The content of Co and B changed slightly as the BN(h) size increased. On the other hand, the related diffraction peaks of the BN(h) nanoparticles were not distinct, probably due to their relatively low content. After comparing Figures 3 and 4, the variation of BN(h) particle size had no obvious effects on the phase, grain size and content.

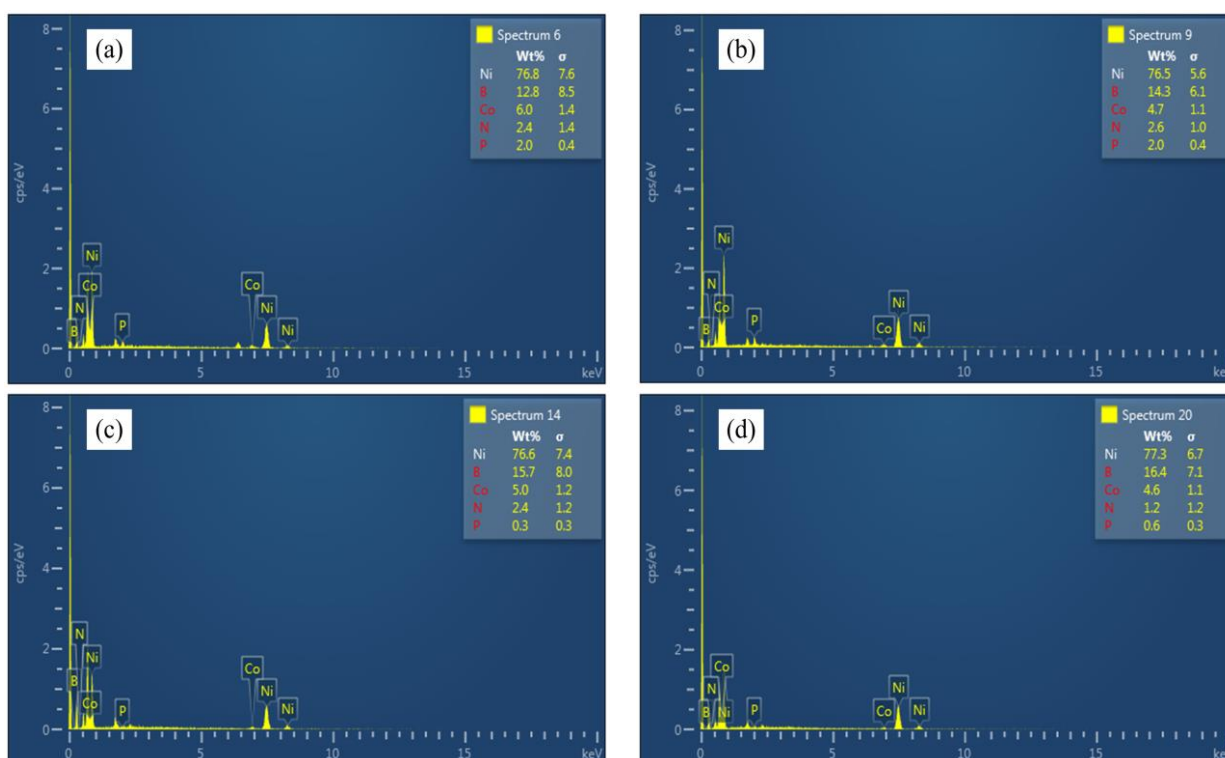
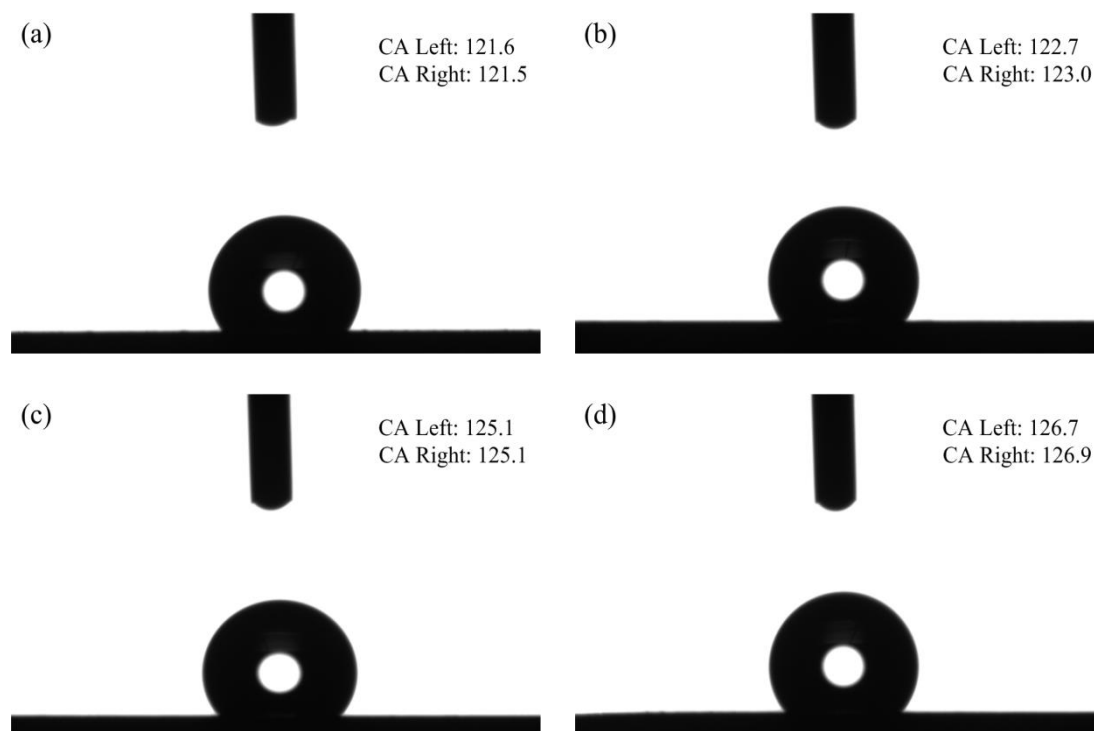


**Figure 4.** EDS spectra of the samples with differently sized BN(h) particles: (a) 50 nm, (b) 100 nm, (c) 500 nm and (d) 800 nm ( $60\text{ }^{\circ}\text{C}$ ,  $6\text{ A}\cdot\text{dm}^{-2}$ , 90 min and 300 rpm).

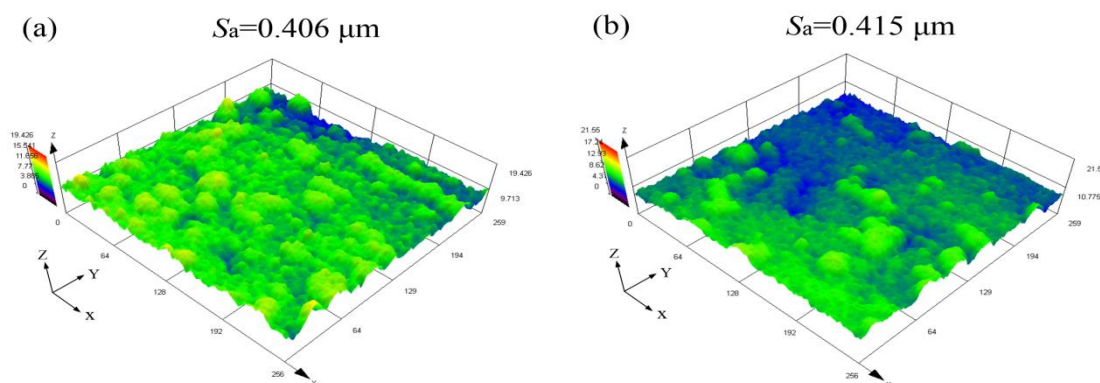
### 3.2 Wettability and surface roughness of the Ni-Co-P-BN(h) nanocomposite coatings

Figure 5 shows the water contact angle of the samples with differently sized BN(h) particles. As shown in Figure 5, the water contact angle increased from  $121.6^{\circ}$  to  $126.7^{\circ}$  when the BN(h) particle size was changed from 50 nm to 800 nm. Weak hydrophobicity was observed on the samples. According to the Wenzel model [42], the roughness factor of the material surface will make a hydrophilic material

even more hydrophilic and a hydrophobic material more hydrophobic. Therefore, to further analyse the effects of the BN(h) particle sizes on the water contact angle of the samples, the surface roughness values of the Ni-Co-P-BN(h) nanocomposite coatings were recorded, as shown in Figure 6. The surface roughness of the Ni-Co-P-BN(h) nanocomposite coatings with BN(h) particle sizes of 50 nm, 100 nm, 500 nm and 800 nm were 0.406  $\mu\text{m}$ , 0.415  $\mu\text{m}$ , 0.451  $\mu\text{m}$  and 0.468  $\mu\text{m}$ , respectively. It was clear that there existed an approximate linear relationship between the apparent contact angle and the roughness factor of the surface, which was consistent with Wenzel’s theory. On the other hand, Wan [43] also reported that the apparent equilibrium contact angle changed from 70.2° to 112.6° with increasing surface roughness.



**Figure 5.** Water contact angle of the samples with differently sized BN(h) particles: (a) 50 nm, (b) 100 nm, (c) 500 nm, and (d) 800 nm (the volume, 3  $\mu\text{L}$ ; the velocity, 1  $\mu\text{L/s}$ ).



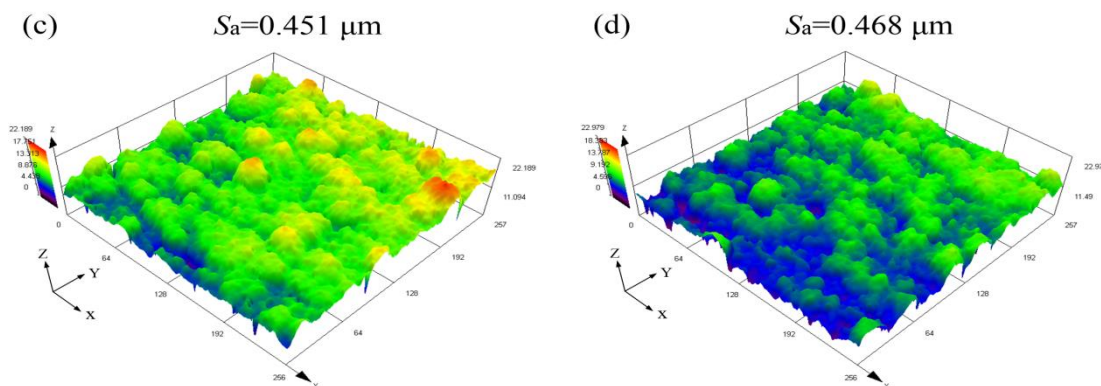


**Figure 6.** Surface roughness of the samples with differently sized BN(h) particles: (a) 50 nm, (b) 100 nm, (c) 500 nm, and (d) 800 nm (the evaluation area, 120 μm×120 μm).

3.3 Fabrication, wettability, surface roughness and anti-adhesion of the superhydrophobic coatings

The previously reported superhydrophobic surface is usually prepared by two typical processes [44]: (1) the fabrication of rough structures and (2) the modification of the rough structures with a low surface energy substance. Figure 7 shows the water contact angle after the samples were modified by only FAS. The water contact angle of the Ni-Co-P-BN(h) nanocomposite coatings with BN(h) particle sizes of 50 nm, 100 nm, 500 nm and 800 nm increased to 130.1°, 133.5°, 136.2° and 138.1°, respectively. It is worth noting that the water contact angle for the coatings improved when the samples were modified by FAS. However, the water contact angle of the sample surfaces cannot reach 150°. The electrochemical machining method is simple and highly effective. Based on ECM technology, Song et al. [45] and Xiang et al. [46] fabricated superhydrophobic surfaces on different metal materials. Li [47] fabricated superhydrophobic Ni-Co alloy coatings on 45 steel substrates. Furthermore, it has been determined that the current density and process time of the ECM play a key role in the regulation of wettability.

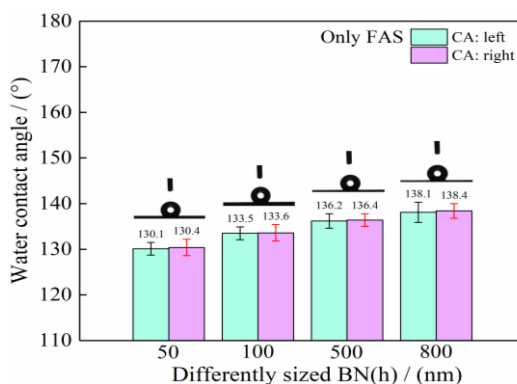


**Figure 7.** Water contact angle after the samples were modified by only FAS (25 °C, 2 h).

Figure 8 shows the effect of electrochemical machining (ECM) current density and process time on the water contact angle of the samples. As shown in Figure 8 (a), the current density of ECM was

increased from 5 A/dm<sup>2</sup> to 25 A/dm<sup>2</sup> under a constant process time of 90 s. When the current density of ECM was 5 A/dm<sup>2</sup>, the water contact angle was only 143.9°. As the current density of the ECM increased, the water contact angle first increased and then decreased. When the current density of the ECM was 15 A/dm<sup>2</sup>, the water contact angle of the samples reached a maximum value of 153.2°. The possible reasons are that the microstructures on the surface of the Ni-Co-P-BN(h) nanocomposite coatings became bumpy as the current density increased. Continually increasing the current density of ECM up to 25 A/dm<sup>2</sup> accelerated the dissolution of the micro/nanostructures. The microstructures on the surface of the samples became flat, which negatively influenced the superhydrophobicity of the sample surfaces [48]. To further analyse the effects of ECM processing time on the wettability of the Ni-Co-P-BN(h) nanocomposite coatings, Figure 8 (b) shows the results when the ECM process time was increased from 0 s to 120 s with a constant current density of 15 A/dm<sup>2</sup>. When the processing times were 0 s, 30 s, 60 s, 90 s and 120 s, the water contact angles were 130.1°, 137.3°, 144.2°, 153.2° and 148.7°, respectively. Therefore, our experiments showed that a suitable processing time with a constant current density of 15 A/dm<sup>2</sup> was 90 s.

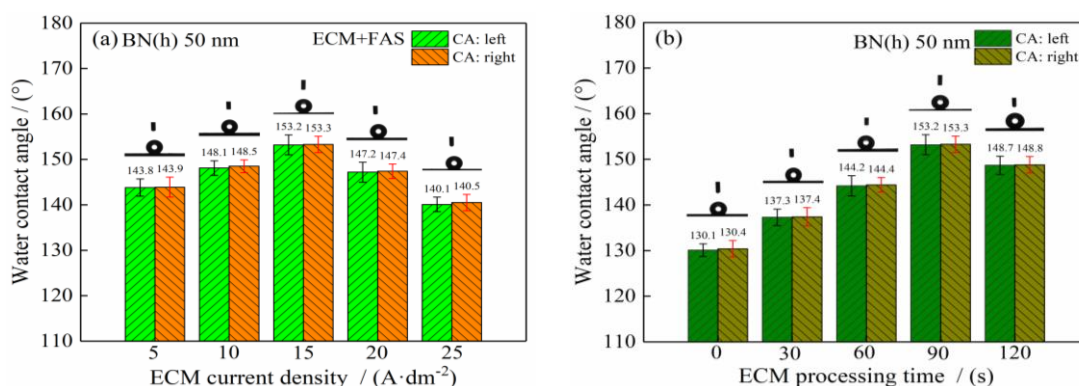


**Figure 8.** Effect of ECM current densities and processing times on the water contact angle of the samples: (a) varying ECM current density (25 °C, 90 s) and (b) varying ECM processing time (25 °C, 15 A/dm<sup>2</sup>). Samples were modified by FAS (25 °C, 2 h) after ECM.

Figure 9 shows the water contact angle of the superhydrophobic coatings with differently sized BN(h) particles when the ECM current density was 15 A/dm<sup>2</sup> and the ECM processing time was 90 s. As shown in Figure 9, the water contact angles of the superhydrophobic coatings with BN(h) particle sizes of 50 nm, 100 nm, 500 nm and 800 nm were 153.2°, 150.3°, 151.1° and 152.3°, respectively. When the samples were treated with FAS after ECM, the water contact angles for the samples with BN(h) particle sizes of 50 nm, 100 nm, 500 nm and 800 nm increased by 31.6°, 27.6°, 26.0° and 25.6°, respectively, compared to those of the untreated samples. Moreover, the fabricated water contact angle exceeded 150°, and the minimum sliding angle corresponded to 5° in the dynamic angle contact test. Hence, a superhydrophobic surface was obtained on the sample surfaces.

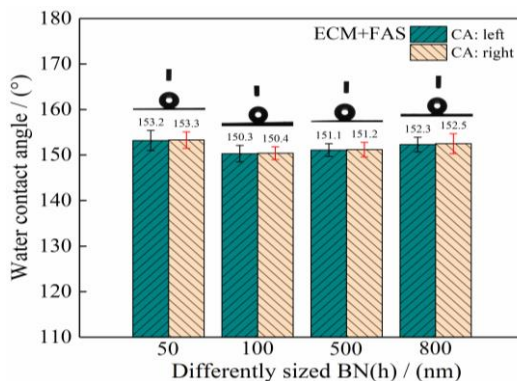


**Figure 9.** Water contact angles of the superhydrophobic coatings with differently sized BN(h) particles: (a) 50 nm, (b) 100 nm, (c) 500 nm, (d) 800 nm (25 °C, 15 A/dm<sup>2</sup>, 90 s). Samples were modified by FAS (25 °C, 2 h) after ECM.

Figure 10 shows the roughness of the superhydrophobic coatings with differently sized BN(h) particles. As shown in the figures, the roughness of the superhydrophobic coatings with BN(h) particle sizes of 50 nm, 100 nm, 500 nm and 800 nm corresponded to 0.974 μm, 0.926 μm, 0.955 μm and 0.961 μm, respectively. Compared to those of the untreated samples, the roughness of the superhydrophobic coatings with BN(h) particle sizes of 50 nm, 100 nm, 500 nm and 800 nm increased by 0.568 μm, 0.511 μm, 0.504 μm and 0.493 μm, respectively. Therefore, our experiments showed that the regulation of ECM changed the original surface roughness. The changes influenced the wettability and improved the water contact angle.

Generally, there are two general models in regard to the effects of surface roughness on wettability: the Wenzel model and the Cassie-Baxter model. The Wenzel model assumes that the non-composite wetting state where the liquid drop fills up the asperities and wets the pillar surface modifies the water contact angle as follows [49-50]:

$$\cos \theta_w = r \cos \theta \tag{1}$$

where  $\theta_w$  and  $\theta$  are the water contact angle of a liquid droplet on a rough surface and a smooth solid surface made of the same material, respectively, and  $r$  is a roughness factor reflecting the surface roughness of a solid. According to previous literature [51],  $r$  is described by the equation:

$$r = \frac{\text{actual surface area}}{\text{planar area}} \tag{2}$$

In particular, when  $r = 1$  the surface is ideally smooth, and the contact angle is only described by Young’s equation (equation (3)): where  $\gamma_{sv}$ ,  $\gamma_{sl}$  and  $\gamma_{lv}$  are the interfacial tensions between solid vapor, solid liquid, and liquid vapor, respectively.

$$\cos \theta = \frac{(\gamma_{sv} - \gamma_{sl})}{\gamma_{lv}} \tag{3}$$

The contact angle can be determined through the Cassie-Baxter equation to better explain the wettability on the surface [52]:

$$\cos \theta_w = f_1 \cos \theta_1 + f_2 \cos \theta_2 \tag{4}$$

where  $\theta_w$  is the apparent contact angle and  $\theta_1$  and  $\theta_2$  are the corresponding intrinsic CAs on each component, and  $f_1$  and  $f_2$  are the surface area fractions of components 1 and 2 ( $f_1 + f_2 = 1$ ), respectively; for a superhydrophobic surface, the second component is trapped air, which means  $\theta_1 = \theta$ ,  $\theta_2 = 180^\circ$ . Thus, equation (4) can be written as follows:

$$\cos \theta_w = f_1 \cos \theta_1 - f_2 = f_1 \cos \theta - 1 + f_1 \quad (5)$$

In addition, the contact angle  $\theta$  is 94.5 degrees, and the Cassie-Baxter contact angle  $\theta_w$  is 153.2 degrees. According to equation (5), it can be estimated that  $f_1$  is approximately 0.116, which demonstrates that air occupies approximately 88.4% of the contact area when a water droplet comes to contact the superhydrophobic surface. This indicates that a large amount of air surrounds the surface of the samples, which reduces the effective area between the water droplet and the solid surface and prevents the water droplet from immersing into the inner surface.

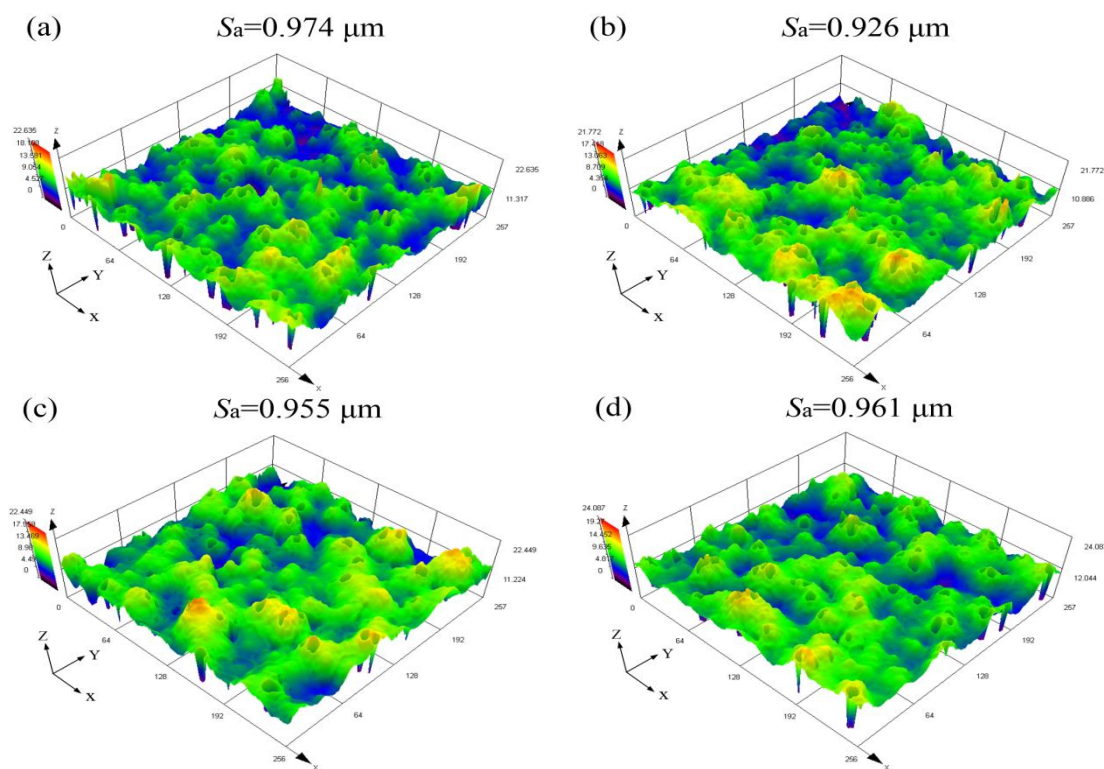


**Figure 10.** Surface roughness values of the superhydrophobic coatings with differently sized BN(h) particles: (a) 50 nm, (b) 100 nm, (c) 500 nm, and (d) 800 nm (the evaluation area,  $120 \mu\text{m} \times 120 \mu\text{m}$ ).

Moreover, Fan [53] reported that the value of  $f_2$  in the system was approximately 0.907, which demonstrated that air occupied approximately 90.7% of the contact areas. Li and Kang [54] found that the area fraction of the air trapped within the interstices of the micro/nanostructures was 87.4%. Zheng [55] reported that the air/water interface occupied 87.5% of the apparent area when the SCSS was in contact with the water droplet. Qing [56] found that air occupied approximately 93.1% of the contact area between the water droplet and micro/nanostructures. Wang [57] reported that the water droplet accounted for only 3.3% contact when it came into contact with a superhydrophobic surface. Li [58]

calculated the fraction of trapped air from equation (5), which was approximately 93% on the superhydrophobic surface. Zou [59] also reported that the  $f_2$  value of a porous microstructure was calculated to be 0.951, denoting that a water droplet had 95.1% of its surface in contact with air between grooves. In this paper, the research results were similar to the above conclusions.

Figure 11 shows sequential images of the water droplets before and after contact with the superhydrophobic coatings. As shown in Figure 11 (a), the water droplet was hung on the microsyringe needle in the initial state. Then, we gradually moved the sample surface upward to contact the 3  $\mu\text{L}$  water droplet, as shown in Figure 11 (b). It is clear that the deformation of the water droplet occurred when the sample surface came into contact with the water droplet. With the surface of the samples continuously moving closer, the water droplet was seriously condensed, and the morphology of the water droplet deformed greatly, as shown in Figure 11 (c) and (d). In the process of compression, the water drop gradually changed from spherical to ellipsoid, and it was difficult to have it fall to the surface in any state in Figure 11 (e). When the sample surface was separated from the water droplet in Figure 11 (f), the water droplet returned to the head of the microsyringe at a slow speed. However, the water droplet did not continue to move with the movement of the samples surface, rather, it still stayed on the tip of the microsyringe in Figure 11 (g) and (h). The results showed that the adhesion between the sample surface and the water droplet was very weak. Thus, the surface has excellent anti-adhesion properties and possesses potential applications in engineering fields, which is consistent with previous reports by Su [60], Song [61], Chen [62] and Yin [63].

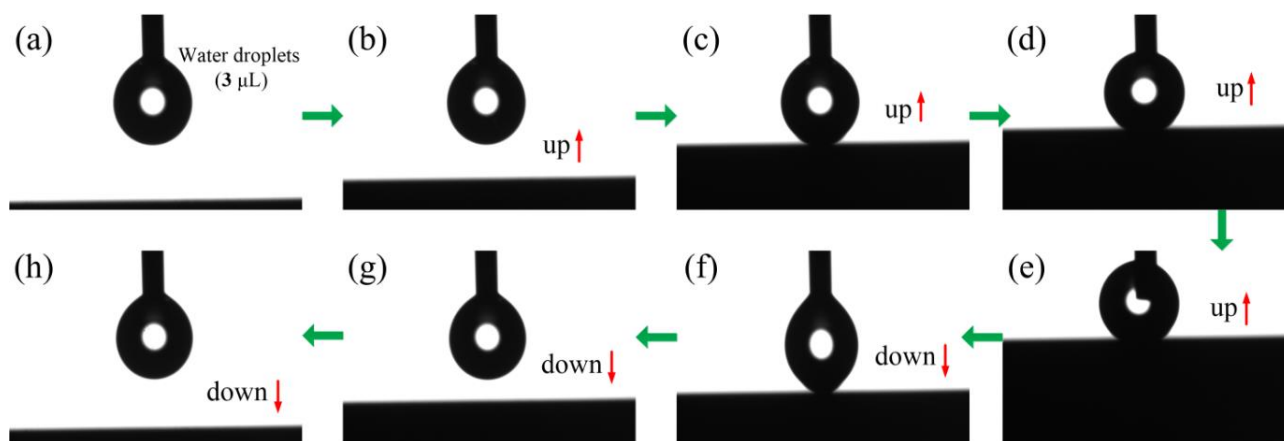


**Figure 11.** Sequential images of a water droplet before and after contact with the superhydrophobic coating: (a and b) initial state, (c) slight contact, (d and e) firm contact, (f) lowering of the surface, (g and h) final state (volume, 3  $\mu\text{L}$ ; velocity, 1  $\mu\text{L/s}$ ).

#### 3.4 Corrosion resistance of the coatings and superhydrophobic coatings

The potentiodynamic polarization curves of the Ni-Co-P-BN(h) nanocomposite coatings and superhydrophobic coatings measured in a 3.5 wt% NaCl solution are shown in Figure 12. The calculated corrosion potentials ( $E_{\text{corr}}$ ), corrosion current densities ( $I_{\text{corr}}$ ) and polarization resistances ( $R_p$ ) obtained

from Figure 12 are listed in Table 2. In a typical polarization curve, a low corrosion current density or a high corrosion potential corresponds to a low corrosion rate and a good corrosion resistance. As described in a previous publication [64], the corrosion potentials and current densities are calculated by the Stern-Geary equation, where  $\beta_a$  and  $\beta_c$  correspond to the anodic and cathodic Tafel slopes, respectively.

$$R_p = \frac{\beta_a \beta_c}{2.3 I_{\text{corr}} (\beta_a + \beta_c)} \quad (6)$$

According to Figure 12 and Table 2, the corrosion current densities ( $I_{\text{corr}}$ ) of the Ni-Co-P-BN(h) nanocomposite coatings with BN(h) particle sizes of 50 nm, 100 nm, 500 nm and 800 nm were 13.44  $\mu\text{A}/\text{cm}^2$ , 12.45  $\mu\text{A}/\text{cm}^2$ , 7.09  $\mu\text{A}/\text{cm}^2$  and 6.99  $\mu\text{A}/\text{cm}^2$ , respectively. The polarization resistances ( $R_p$ ) of the samples with BN(h) particle sizes of 50 nm, 100 nm, 500 nm and 800 nm increased to 4.86  $\text{k}\Omega \cdot \text{cm}^2$ , 6.96  $\text{k}\Omega \cdot \text{cm}^2$ , 6.31  $\text{k}\Omega \cdot \text{cm}^2$  and 10.46  $\text{k}\Omega \cdot \text{cm}^2$ , respectively. Compared with the normal samples, the corrosion current densities of the coatings treated by FAS exhibited lower corrosion current density and higher polarization resistance. The above phenomena might be explained from Figure 7 and Figure 9; the water contact angle increased when the BN(h) particle size was changed from 50 nm to 800 nm. At the same time, the water contact angle further increased after the samples were modified by FAS. Although the corrosion resistances of the coatings treated by FAS were better compared to that of the untreated samples, the samples with superhydrophobic surfaces exhibited the best performances in terms of both corrosion current density ( $I_{\text{corr}}$ ) and polarization resistance ( $R_p$ ). In addition, when the BN(h) particle size was 800 nm, the corrosion current density ( $I_{\text{corr}}$ ) of the superhydrophobic coatings reached a minimum value of 0.14  $\mu\text{A}/\text{cm}^2$  and the polarization resistance ( $R_p$ ) reached a maximum value of 131.40  $\text{k}\Omega \cdot \text{cm}^2$ . Such low current density and high polarization resistance showed that corrosion resistance was greatly improved. This result was consistent with other studies showing that superhydrophobic surfaces could improve corrosion resistance [65-68].

Herein, the above results could be explained by the Wenzel–Cassie model. The theory of the Wenzel-Cassie model states that the interface between the liquid and solid material with microstructures is a complex interface that consists of solids, air, and liquids, as shown in Figure 13. The superhydrophobic coatings exhibited the smallest solid-liquid interface in a 3.5 wt% NaCl solution. In addition, this could form a protective “air cushion” layer on the surface of the superhydrophobic coating, which made it difficult for  $\text{Cl}^-$  to get close to the superhydrophobic coatings in the corrosion solution. Thus, it exhibited the lowest corrosion current density and highest corrosion potential. Moreover, Ou et al. [69] also showed that Mg-H<sub>2</sub>O-(PA/Ce)n-HDMS had much better corrosion resistance due to retaining a thin layer of air at the solid/water interface in the NaCl aqueous solution.

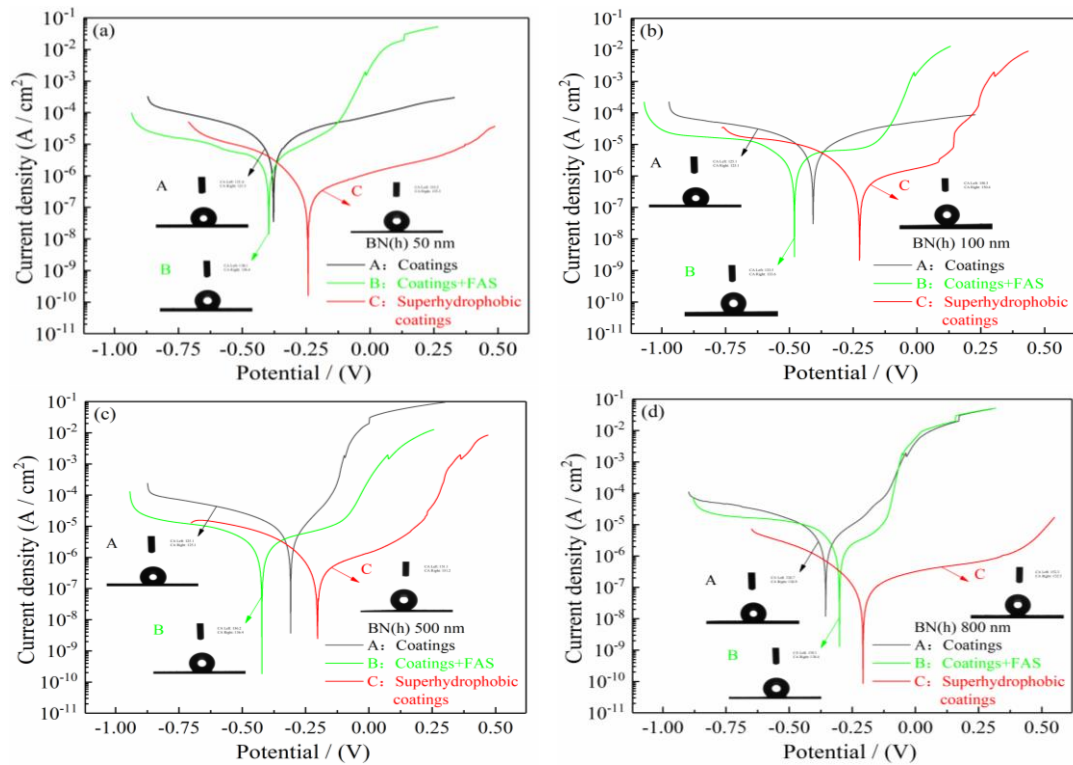


**Figure 12.** Potentiodynamic polarization curves of the samples in a 3.5 wt% NaCl aqueous solution (scanning range,  $-0.6\text{ V} \sim +0.6\text{ V}$  with respect to  $E_{ocp}$ ; scan rate,  $0.5\text{ mV/s}$ ).

**Table 2.** Corrosion potentials ( $E_{corr}$ ) and corrosion current densities ( $I_{corr}$ ) obtained from the polarization curves and polarization resistances ( $R_p$ ) calculated by equation (6)

Samples		$\beta_a$ (mV/dec)	$\beta_c$ (mV/dec)	$I_{corr}$ ( $\mu\text{A}/\text{cm}^2$ )	$E_{corr}$ (mV)	$R_p$ ( $\text{k}\Omega \cdot \text{cm}^2$ )
BN(h) 50 nm	coatings	356	260	13.44	-378	4.86
	coatings+FAS	428	838	8.67	-396	14.21
	superhydrophobic coatings	263	101	0.28	-243	113.32
BN(h) 100 nm	coatings	478	342	12.45	-407	6.96
	coatings+FAS	649	411	7.67	-480	14.26
	superhydrophobic coatings	770	161	0.61	-225	94.91
BN(h) 500 nm	coatings	169	263	7.09	-308	6.31
	coatings+FAS	701	422	5.89	-422	19.44
	superhydrophobic coatings	139	83	0.23	-203	98.24
BN(h) 800 nm	coatings	395	293	6.99	-355	10.46
	coatings+FAS	472	228	4.98	-301	13.42
	superhydrophobic coatings	112	68	0.14	-207	131.40

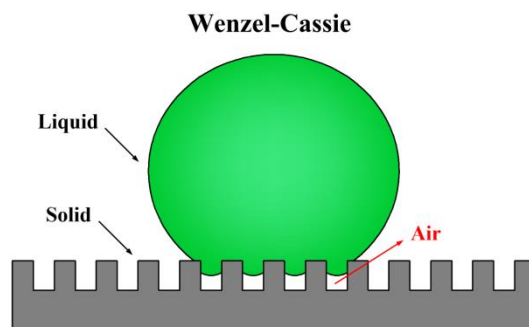


**Figure 13.** Hydrophobicity model proposed by Wenzel–Cassie

#### 4. CONCLUSION

In this work, a superhydrophobic surface was fabricated on 45 steel substrates by using electrochemical machining and fluorosilane modification. The results showed that the electrochemical machining current density and processing time significantly influenced wettability. The Ni-Co-P-BN(h) nanocomposite coatings exhibited a superhydrophobic surface under suitable process parameters. Evaluation of this superhydrophobic surface revealed an average water contact angle of  $153.2^\circ$  and a sliding angle of  $5^\circ$  in the contact angle test. In addition, the polarization curve in the electrochemical test indicated that the superhydrophobic surface also exhibited a lower corrosion current density ( $I_{\text{corr}}$ ) of  $0.14 \mu\text{A}/\text{cm}^2$  and a higher polarization resistance ( $R_p$ ) of  $131.40 \text{ k}\Omega \cdot \text{cm}^2$  compared with those of the normal samples. Thus, the above results showed that Ni-Co-P-BN(h) nanocomposite coatings with superhydrophobic surfaces could provide improved corrosion resistance.

#### ACKNOWLEDGEMENTS

The authors would like to acknowledge the Research and Innovation Program for Graduate Students in Jiangsu, Grant No. KYCX19\_0607 and the Technology Development Programme for the Northern Jiangsu area, Grant No. BN2014019.

#### CONFLICTS OF INTEREST

The authors declare no conflicts of interest.

#### References

1. G. Zhang, Q. Xie, C. Ma and G. Zhang. *Prog. Org. Coat.*, 117 (2018) 29.
2. E. Vazirinas, R. Jafari and G. Momen. *Surf. Coat. Technol.*, 341 (2018) 40.
3. M. Ramezanzadeh, G. Bahlakeh, Z. Sanaei, and B. Ramezanzadeh. *J. Ind. Eng. Chem.*, 74 (2019) 26.
4. J. Pang, Q. Li, W. Wang, X. Xu, and J. Zhai. *Surf. Coat. Technol.*, 205 (2011) 4237.
5. A.E. Fetohi, R.M.A. Hameed, K.M. El-Khatib and R. Souaya Eglal. *Int. J. Hydrogen Energy*, 37 (2012) 7677.
6. W.T. Chiu, C.Y. Chen, T.F.M. Chang, T. Hashimoto, H. Kurosu and M. Sone. *Electrochim. Acta*, 294 (2019) 68.
7. O.S.I. Fayomi, A.A. Atayero, M P. Mubiayi, I.G. Akande, P.A. Adewuyi, M.A. Fajobi, W.A. Ayara, and A.P.I. Popoola. *J. Alloys Compd.*, 773 (2018) 305.
8. M.S. Mehr, A. Akbari and E. Damerchi. *J. Alloys Compd.*, 782 (2019) 477.

9. J. Du, L. Wang, L. Bai, S. Dang, L. Su, X. Qin and G. Shao. *J. Colloid Interface Sci.*, 535 (2019) 75.
10. A. Bahrami, I. Kazeminezhad and Y. Abdi. *Superlattices Microstruct.*, 125 (2019) 125.
11. B. Li, D. Li, T. Mei, W. Xia and W. Zhang. *J. Alloys Compd.*, 777 (2019) 1234.
12. B. Li, W. Zhang, D. Li, Y. Huan and J. Dong. *Appl. Surf. Sci.*, 458 (2018) 305.
13. L.Y. Cui, G.B. Wei, Z.Z. Han, R.C. Zeng, L. Wang, Y.H. Zou, S.Q. Li, D.K. Xu and S.K. Guan. *J. Mater. Sci. Technol.*, 35 (2019) 254.
14. S. Ammara, S. Shamaila, N. Zafar, A. Bokhari and A. Sabah. *J. Phys. Chem. Solids*, 120 (2018) 12.
15. B. Li and W. Zhang. *Ceram. Int.*, 44 (2018) 19907.
16. H. Li, Y. He, T. He, D. Qing, F. Luo, Y. Fan and X. Chen. *J. Alloys Compd.*, 704 (2017) 32.
17. A. Hooda, M.S. Goyat, A. Kumar and R. Gupta. *Mater. Lett.*, 233 (2018) 340.
18. M.M. Hossain, Q.H. Trinh, D.B. Nguyen, M.S.P. Sudhakaran and Y.S. Mok. *Thin Solid Films*, 675 (2019) 34.
19. X. Lin, S. Park, D. Choi, J. Heo and J. Hong. *J. Ind. Eng. Chem.*, 74 (2019) 79.
20. Y. Li, L. Gou, H. Wang, Y. Wang, J. Zhang, N. Li, S. Hu and J. Yang. *Mater. Lett.*, 244 (2019) 31.
21. R. Cai, K. Glinel, D. De Smet, M. Vanneste, N. Mannu, B. Kartheuser, B. Nysten and A.M. Jonas. *ACS. Appl. Mater. Interfaces*, 10 (2018) 15346.
22. J. Yang, P. Xu, Y. Xia and B. Chen. *Cellul.*, 25 (2018) 5863.
23. M.J. Coady, M. Wood, G.Q. Wallace, K.E. Nielsen, A.M. Kietzig, F. Lagugne Labarthe and P.J. Ragona. *ACS. Appl. Mater. Interfaces*, 10 (2018) 2890.
24. Y. Tuo, W. Chen, H. Zhang, P. Li and X. Liu. *Appl. Surf. Sci.*, 446 (2018) 230.
25. J. Huang, S. Lyu, Z. Chen, S. Wang and F. Fu. *J. Colloid Interface Sci.*, 536 (2019) 349.
26. P. Wang, D. Zhang, Z. Lu and S. Sun. *ACS. Appl. Mater. Interfaces*, 8 (2016) 1120.
27. C. Anitha, S. Syed Azim, S. Mayavan. *Appl. Surf. Sci.*, 449 (2018) 250.
28. Q. Wan, G. Chen, J. Tian, Z. Yu, Q. Deng and M. Yu. *Mater. Lett.*, 230 (2018) 84.
29. Y. Lin, J.P. Han, M.Y. Cai, W.J. Liu, X. Luo, H.J. Zhang and M.L. Zhong. *J. Mater. Chem. A*, 6 (2018) 9049.
30. Y. Yang, X. Li, X. Zheng, Z. Chen, Q. Zhou and Y. Chen. *Adv. Mater.*, 30 (2018) 1870062.
31. Y. Wu, S. Jia, Y. Qing, S. Luo and M. Liu. *J. Mater. Chem. A*, 4 (2018) 14111.
32. Z. Lin, H. Li, X. Lai, X. Su, L. Tao and X. Zeng. *Chem. Eng. J.*, 316 (2017) 736.
33. F. Hizal, N. Rungraeng, J. Lee, S. Jun, H.J. Busscher, V.D.M. Hc and C.H. ACS. *Appl. Mater. Interfaces*, 9 (2017) 12118.
34. R. Di Mundo, F. Bottiglione and G. Carbone. *Appl. Surf. Sci.*, 316 (2014) 324.
35. C.H. Xue, Y.R. Li, P. Zhang, J.Z. Ma and S.T. Jia. *ACS. Appl. Mater. Interfaces*, 6 (2014) 10153.
36. A. Kumar and B. Gogoi. *Tribol. Int.*, 122 (2018) 114.
37. H. Wang, G. Chi, Y. Wang, F. Yu and Z. Wang. *Appl. Surf. Sci.*, 478 (2019) 110.
38. J. Liang, D. Li, D. Wang, K. Liu and L. Chen. *Appl. Surf. Sci.*, 293 (2014) 265.
39. Y. Liu, X. Yin, J. Zhang, S. Yu, Z. Han and L. Ren. *Electrochim. Acta*, 125 (2014) 395.
40. Y. Liu, J. Xue, D. Luo, H. Wang, X. Gong, Z. Han and L. Ren. *J. Colloid Interface Sci.*, 491 (2017) 313.
41. Y. Zhong, J. Hu, Y. Zhang and S. Tang. *Appl. Surf. Sci.*, 427 (2018) 1193.
42. J. Kuang, Z. Ba, Z. Li, Y. Jia and Z. Wang. *Surf. Coat. Technol.*, 361 (2019) 75.
43. B. Wan, H. Zhang, M. Gao, P. Bai and H. Zhang. *Mater. Design*, 138 (2017) 103.
44. Z. Qian, S. Wang and X. Ye. *Appl. Surf. Sci.*, 453 (2018) 1.
45. J.L. Song, W.J. Xu, Y. Lu, X. Liu, Z.F. Wei and J. Sun. *J. Mech. Eng.*, 49 (2018) 182.
46. T. Xiang, Y. Han, Z. Guo, R. Wang, S. Zheng, S. Li, C. Li and X. Dai. *ACS. Sustainable Chem. Eng.*, 6 (2018) 5598.
47. H. Li, M. Kang, Y. Zhang, Y. Liu, M. Jin, S.N. Mbugua, G. Zhu and C. Liu. *Nanosci. Nanotech. Lett.*, 11 (2019) 1.
48. H. Zhang, L. Yin, S. Shi, X. Liu, Y. Wang and F. Wang. *Microelectron. Eng.*, 141 (2015) 238.

49. C. Weng, F. Wang, M. Zhou, D. Yang and B. Jiang. *Appl. Surf. Sci.*, 436 (2018) 224.
50. L. Feng, Y. Che, Y. Liu, X. Qiang and Y. Wang. *Appl. Surf. Sci.*, 283 (2013) 367.
51. A.T. Abdulhussein, G.K. Kannarpady, A.B. Wright, A. Ghosh and A.S. Biris. *Appl. Surf. Sci.*, 384 (2016) 311.
52. J.H. Kim, A. Mirzaei, H. Woo Kim and S. Sub Kim. *Appl. Surf. Sci.*, 439 (2018) 598.
53. Y. Fan, C. Li, Z. Chen, F. Ma and H. Chen. *Surf. Coat. Technol.*, 213 (2012) 8.
54. W. Li and Z. Kang. *Surf. Coat. Technol.*, 253 (2014) 205.
55. S. Zheng, C. Li, Q. Fu, M. Li, W. Hu, Q. Wang, M. Du, X. Liu and Z. Chen. *Surf. Coat. Technol.*, 276 (2015) 341.
56. Y. Qing, C. Yang, Y. Sun, Y. Zheng, X. Wang, Y. Shang, L. Wang and C. Liu. *Colloids Surf. A*, 484 (2015) 471.
57. L. Wang, H. Li, J. Song and Y. Sun. *Surf. Coat. Technol.*, 302 (2016) 507.
58. J. Li, F. Du, Y. Zhao, S. Zhao and H. Yu. *Opt. Laser. Technol.*, 113 (2019) 273.
59. Y. Zou, Y. Wang, S. Xu, T. Jin, D. Wei, J. Ouyang, D. Jia and Y. Zhou. *Chem. Eng. J.*, 362 (2019) 638.
60. C. Su, Z. Lu, H. Zhao, H. Yang and R. Chen. *Appl. Surf. Sci.*, 353 (2015) 735.
61. J. Song, D. Wang, X. Huang and Y. Chen. *Appl. Surf. Sci.*, 455 (2018) 771.
62. K. Chen, J. Zhou, F. Ge, R. Zhao and C. Wang. *Colloids Surf. A*, 565 (2019) 86.
63. X. Yin, S. Yu, J. Hu, H. Li, Z. Lv and X. Zhou. *J. Alloys Compd*, 791 (2019) 64.
64. W. Xu, K. Rajan, X. Grant Chen, D.K. Sarkar. *Surf. Coat. Technol.*, 364 (2019) 406.
65. P. Wang, T. Yao, B. Sun, X. Fan, S. Dong, Y. Bai and Y. Shi. *Colloids Surf. A*, 513 (2017) 396.
66. F. Zhang, C. Zhang, L. Song, R. Zeng, S. Li and H. Cui. *J. Mater. Sci. Technol.*, 31 (2015) 1139.
67. X. Zhang, J. Zhao, J. Mo, R. Suna, Z. Li and Z. Guo. *Colloids Surf. A*, 567 (2019) 205.
68. H. Zhou, R. Chen, Q. Liu, J. Liu, J. Yu, C. Wang, M. Zhang, P. Liu and J. Wang. *Chem. Eng. J.*, 368 (2019) 261.
69. J. Ou and X. Chen. *J. Alloys Compd*, 787 (2018) 145.

© 2020 The Authors. Published by ESG ([www.electrochemsci.org](http://www.electrochemsci.org)). This article is an open access article distributed under the terms and conditions of the Creative Commons Attribution license (<http://creativecommons.org/licenses/by/4.0/>).